Modelling a feather as a strongly anisotropic elastic shell: supplementary information

Jean Jouve
Univ. Grenoble Alpes, Inria, CNRS, Grenoble INP, LJK
Grenoble, France
jean.jouve@inria.fr

Victor Romero
Univ. Grenoble Alpes, Inria, CNRS, Grenoble INP, LJK
Grenoble, France
victor.romero-gramegna@inria.fr

Rahul Narain
Indian Institute of Technology Delhi
New Delhi, India
narain@cse.iitd.ac.in

Laurence Boissieux
Univ. Grenoble Alpes, Inria
Grenoble, France
laurence.boissieux@inria.fr

Theodore Kim
Yale University
New Haven, United States of America
theodore.kim@yale.edu

Florence Bertails-Descoubes
Univ. Grenoble Alpes, Inria, CNRS, Grenoble INP, LJK
Grenoble, France
florence.descoubes@inria.fr

ACM Reference Format:
Jean Jouve, Victor Romero, Rahul Narain, Laurence Boissieux, Theodore Kim, and Florence Bertails-Descoubes. 2024. Modelling a feather as a strongly anisotropic elastic shell: supplementary information. In *Special Interest Group on Computer Graphics and Interactive Techniques Conference Conference Papers '24 (SIGGRAPH Conference Papers '24), July 27-August 1, 2024, Denver, CO, USA.* ACM, New York, NY, USA, 12 pages. https://doi.org/10.1145/3641519.3657503

Contents

SIGGRAPH Conference Papers '24, July 27-August 1, 2024, Denver, CO, USA

ACM ISBN 979-8-4007-0525-0/24/07.
https://doi.org/10.1145/3641519.3657503

1 INTRODUCTION

We gather here some additional computations and information complementing the main paper "Modelling a feather as a strongly anisotropic elastic shell".

2 EXPERIMENTAL SETUP: DETAILS

In this section, we provide a detailed description of the used devices and give the precision for the measuring captors in our experimental setup.

Quasi-static traction experiments are carried out by means of a motorized translational stage Zaber X-LRT0500BL-E08C, which allows us to control the pulling position to an accuracy of $\pm 1\mu$m. Simultaneously, we measure the traction force with a load cell. Depending on the orientation of the barbs, forces may vary widely. For hundreds of milli-Newtons, we use a Futek LBS-200 with a maximum load of 5 N and an accuracy of ±25 mN. For unit Newtons, we measure with a force gauge ME-systems KD-80s with a maximum load of 100 N and an accuracy of ±0.5 N. The signals from the load sensors are acquired by a Ni DAQ at 16 bits and sampled at high frequencies to produce statistically significant measurements. Finally, each run of a traction experiment is imaged at the patch scale with a camera mounted on a microscope Leica z16.

The geometries of the sample used in the traction tests are given in Table 1

3 SOLVING A NONLINEAR PROBLEM

Since the dynamics is time-discretised through an implicit solver and the elasticity is modelled through a nonlinear model, the time-stepping problem takes the form of a system of nonlinear equations. In the original ARCSim code, the time-stepping problem is linearised and solved through a linear system solver [Narain et al. 2012], which is more or less equivalent to performing a single step of the Newton method. Linearisation can be sufficient if the problem is only mildly nonlinear and well-conditioned. However, as shown in Figure 6 in the main paper, the time-stepping problem becomes ill-conditioned when modelling highly anisotropic materials. For this reason we solve our time-stepping problem using a full nonlinear solver.

	l_x [mm]	l_y [mm]	h [µm]
	9	18	73
	7	15	133
	9	23	60
	8	13	120
	9	16	129
	4	12	116
	10	11	80
	7	19	125
	10	10	117
	7	7	100
	7	10	145
	2	7	130
	6	11	140

(a) Geometry of the samples used in the experimental longitudinal traction scenario.

	l_x [mm]	l_y [mm]	h [µm]
	15	14	120
	8	14	100
	12	11	120
	10	11	110
	10	13	95
	12	11	140
	11	13	120
	10	15	100
	17	14	112
	10	13	125
	11	12	120
	16	12	150
	8	10	110
	11	12	120

(b) Geometry of the samples used in the experimental transverse traction scenario.

Table 1: Geometries of the samples used in the experiments. the legend corresponds to Figure 13 in the main document.

While we mitigate the conditioning through the introduction of a constraint, the use of the nonlinear solver is still of importance to properly solve this constraint (See Figure 1).

As mentioned in the main document, we use Ipopt to solve the time-stepping problem [Wächter and Biegler 2006]. This solver is dedicated to nonlinear optimisation problems under constraints. Hence, to interface the solver with our constrained time-stepping problem, we need to rephrase our problem as the search of an optimum. We describe below how we proceed to do so.

We perform the derivation on a time-stepping problem which only considers elasticity and dynamics. The extension to other aspects of ARCSim is straightforward. The Euler-Lagrange equations of the first kind, discretised in space using a finite element method

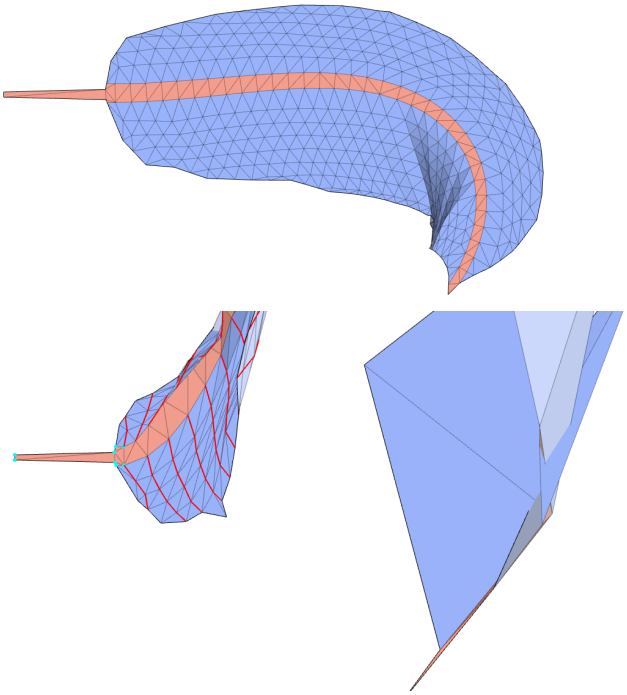

Figure 1: The use of a nonlinear solver is necessary to properly simulate our numerical model (top). When only one nonlinear solver step is used, the behaviour diverges from a realistic one (bottom).

and discretised in time using an implicit Euler method, yield

$$\mathbf{M}\Delta\mathbf{v} = -h\frac{\partial W}{\partial \mathbf{x}}(\mathbf{x}_{n+1}) + h\left(\frac{\partial \mathbf{g}}{\partial \mathbf{x}}(\mathbf{x}_{n+1})\right)^T \lambda;$$
$$\mathbf{g}(\mathbf{x}_{n+1}) = \mathbf{0},$$

where h is the time-step size, $\Delta\mathbf{v} = \mathbf{v}_{n+1} - \mathbf{v}_n$, $\mathbf{x}_{n+1} = \mathbf{x}_n + h\mathbf{v}_{n+1}$, $\mathbf{v}_n$ (resp. $\mathbf{x}_n$) is the discretised velocity (resp. position) at the time t_n, $W(\mathbf{x})$ is the potential elastic energy of the system at position $\mathbf{x}$, $\mathbf{g}(\mathbf{x}) = 0$ is an equality constraint (inextensibility constraint in our case, see section 5 for more details) and λ is its associated Lagrange multiplier.

This initial problem can be reformulated as the optimisation problem we give to Ipopt as,

$$\min_{\substack{\Delta\mathbf{v} \\ \mathbf{g}(\mathbf{x}_{n+1})=\mathbf{0}}} \frac{1}{2}\Delta\mathbf{v}\mathbf{M}\Delta\mathbf{v} + W(\mathbf{x}_{n+1}).$$

4 LOCKING

Specific objects such as thin elastic plates and shells, or incompressible elastic solids and fluids, display materials properties or geometry with extreme disparities. The numerical modelling of scenarios involving such objects through the finite element method (FEM) can be quite costly and sometimes even impossible if some precautions are not taken when choosing the elements to be used. With inappropriate elements, the FEM may converge very slowly,

meaning that a huge number elements may be necessary to get close to a proper accuracy suitable for the target application. Moreover, slow convergence may worsen as geometrical or material parameters become extreme, e.g. a vanishing plate thickness or a Poisson ratio raising to 0.5 (incompressible limit). *Numerical locking* precisely refers to the degradation of numerical convergence as a geometrical or physical parameter tends to a limit value [Brezzi and Fortin 1991].

We show in Figure 2 that a naive discretisation of our strongly anisotropic membrane model yields a locking phenomenon due to the extreme difference between the stiffness of the two principal orientations of the material. Yet, using appropriate elements, and in particular elements that are aligned along the stiffest orientation (that of the barbs), can fix this issue.

5 CONSTRAINT

As seen in the previous section and in the main document, if the elements are not appropriately chosen, the discretisation of our model is subject to numerical locking as the stiffness ratio rises up. However, even if the elements used prevent numerical locking, a high stiffness ratio increases the conditioning of the nonlinear problem solved at each time-stepping. This increased conditioning makes the nonlinear solver particularly slow. We solve this issue by replacing the stiff orientation with a constraint (see Figure 6 in the main document).

In this section we discuss how this constraint was implemented.

For a material which cannot deform along a local orientation $\mathbf{d}$, the barb orientation in our case, the obvious constraint is

$$\mathbf{d}(\mathbf{r}) \cdot \epsilon(\mathbf{r}) \cdot \mathbf{d}(\mathbf{r}) = 0, \forall \mathbf{r} \in \Omega, \tag{1}$$

where Ω is the reference configuration, $\mathbf{r}$ is a material point, $\mathbf{d}(\mathbf{r})$ and $\epsilon(\mathbf{r})$ are respectively the barb orientation and the Green-Lagrange strain at the material point $\mathbf{r}$.

However, it turns out that the Jacobian of the straightforward finite element discretisation of this constraint is not full rank for triangular linear elements. This indicates either an incompatibility or redundancy in the discretised constraints.

Hence, instead, we choose to introduce this constraint through a geometric intuition. Due to the presence of numerical locking, we build a mesh whose edges are along the stiffest orientation. We use this property and introduce constraints that prevent the length of those edges to change throughout the simulation. This means that for each triangle τ in the reference configuration, there is an edge whose vector $\mathbf{E}_\tau$ is collinear to the local stiffest orientation $\mathbf{d}_\tau$. Denoting the deformed edge by $\mathbf{e}_\tau$, the constraint can be written as

$$\|\mathbf{E}_\tau\|^2 = \|\mathbf{e}_\tau\|^2, \forall \tau. \tag{2}$$

Geometrically, it is clear that these constraints are compatible.

Thanks to our use of triangular linear elements, we can show that there is a link between these constraints and the constraints obtained by discretising Equation 1.

For a given triangular linear element τ, we have,

$$\mathbf{F}_\tau \mathbf{E}_\tau = \mathbf{e}_\tau, \tag{3}$$

where $\mathbf{F}_\tau$ is the deformation gradient on the element which is constant over the triangle since we are considering linear elements.

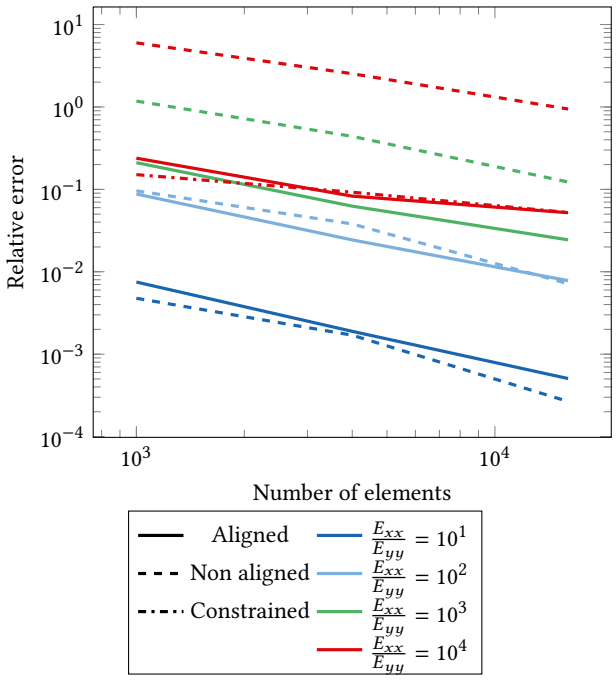

Figure 2: Finite element convergence of the simulated tilted traction scenario with barbs at 45° for different type of meshes and stiffness ratios $\frac{E_{xx}}{E_{yy}}$. Meshes are either aligned (——) or unaligned (- - -) with the orientation of barbs. The error is computed as the relative difference between the evaluated stress at 5 % strain and the same stress for a simulation with aligned mesh and 128×10^3 elements. In addition to those two types of simulations, there is the special case of the aligned mesh with added constraint (-·-·-·), whose behaviour does not depend on the stiffness ratio (see section 5). Its value is compared with the reference for the stiffness ratio $\frac{E_{xx}}{E_{yy}} = 10^4$. As suggested by Chapelle's methodology [1995], these plots clearly show a numerical locking phenomenon when an unaligned mesh is used: the convergence of the finite element method substantially deteriorates as the stiffness ratio is increased. In contrast, the use of an aligned mesh drastically reduces this degradation of convergence.

Due to the norm equality between $\mathbf{E}_\tau$ and $\mathbf{e}_\tau$, this can be written as

$$\mathbf{F}_\tau \mathbf{E}_\tau = \mathbf{R}_\tau \mathbf{E}_\tau, \tag{4}$$

where $\mathbf{R}_\tau$ is a rotation matrix. Using this relation and the equality between the stiffest orientation $\mathbf{d}_\tau$ and $\mathbf{E}_\tau$, we can compute the strain in the stiffest orientation

$$\mathbf{d}_\tau \cdot \epsilon_\tau \cdot \mathbf{d}_\tau = {\mathbf{E}_\tau}^T \frac{1}{2} ({\mathbf{F}_\tau}^T \mathbf{F}_\tau - \mathbf{I}) \mathbf{E}_\tau = 0. \tag{5}$$

This last equation is exactly the finite element discretisation of Equation 1. This shows that constraining the length of edges along the stiffest orientation is equivalent to a constraint on the strain. Moreover, it also demonstrates that the discretisation of Equation 1

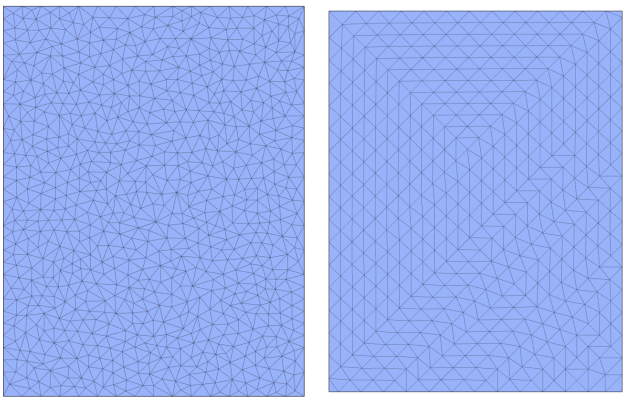

(a) Non aligned mesh (b) Aligned mesh

Figure 3: Examples of meshes used for the simulation of the vane samples. Those are meshes used for the tilted scenario. We either used mesh whose elements are not aligned with the barb direction (left) or mesh whose elements are aligned with those directions (right).

is redundant rather than incompatible, as we have found a reduced number of constraints that do the same.

6 FEATHER MESHING ALGORITHM

In section 4 and in section 6 of the main document, we showed that having elements aligned with the orientation of barbs allows reaching greater accuracy for the same number of elements compared to unaligned elements. Since our tested sample are chosen such that their barbs' orientation is as uniform as possible, producing appropriate mesh representing the sample for the sake of validation was pretty straightforward. However, producing such a mesh for the visual comparison with a real feather is not as easy. As can be seen in the photos at the top of Figure 12, the barb orientation is not uniform across the vane. Hence, our software must provide a way to input barbs' orientation and produce a mesh whose elements are aligned with the given orientations.

The input to our meshing algorithm is (i) the shape of the feather, (ii) the shape of the rachis, and (iii) several *barb curves* on either side of the rachis. All of these are considered to lie in 2D reference space. In our implementation, the feather shape is given as a triangular mesh, of which we only consider the boundary (though in principle, the shape could be given as a closed curve as well). The rachis is specified by a curve defining its centerline, and its start and end width. The barb curves describe the orientations of barbs across the feather surface. Both rachis and barb curves are treated as if they extend until the feather boundary, extrapolated linearly if necessary. Finally, we also take as input a target element's edge length e to control the mesh resolution.

First, we mesh the rachis as a triangulated strip. To do so, we walk along the rachis curve with steps of length e, and create a vertex on either side according to the desired thickness. The thickness is linearly interpolated from the specified starting and ending thicknesses along the length of the rachis curve. Adjacent vertices created in this process are linked with edges.

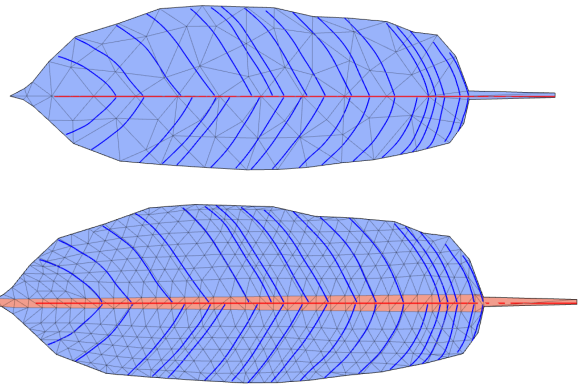

Figure 4: Input (top) and output (bottom) of the meshing component of the software. The input of the software is a mesh (light blue mesh) splines describing the barb orientations (solid blue lines) and another spline describing the position of the rachis (solid red line). The resulting mesh has a central area mesh arbitrarily following the rachis spline for the rachis material (orange area) on either side of this area is the vane (light blue) meshed such that the elements are aligned with barbs orientations.

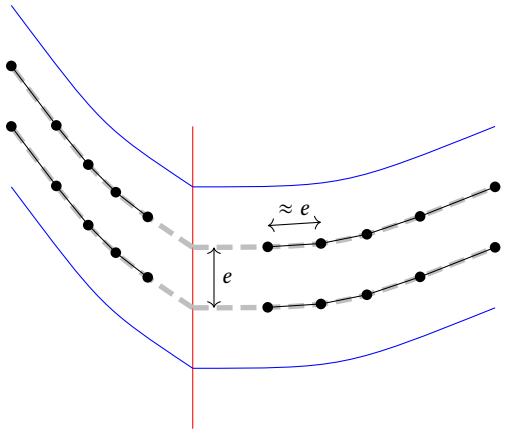

Figure 5: Schematic showing how the meshing algorithm places edges along the barb direction. Starting from the vertices generated for the rachis (——), a barb curve (– –) is interpolated from the closest input curves (——). Then, nodes (●) separated by a distance e and linked by edges (——) along these generated splines.

This generated triangle strip splits the feather into two regions that altogether represent the vane. In these regions, we create vertices and edges along barb directions. From each rachis vertex, we interpolate the closest barb curves. The barb curves from the other vane (i.e. the opposite side of the rachis) must not be considered in this interpolation. On this interpolated curve we walk again in steps of length e until we meet the feather boundary. Adjacent vertices along each such path are linked with edges (see Figure 5).

From this collection of vertices and barb-aligned edges, the final mesh is obtained using constrained Delaunay triangulation computed by Triangle [Shewchuk 1996].

7 NUMERICAL PARAMETERS

In this section, we describe in more details how the values of the different parameters of our simulations have been chosen. The final values are also given.

There are two kinds of scenarios and, hence, two different sets of parameters which have to be chosen through different means. On the one hand we consider traction tests of various feather samples. On the other hand, we deal with the deformation of a full feather.

7.1 Traction Test

The parameter values we used for the figures involving the traction test are listed in Table 4. In what follows, we give a succinct reasoning behind the chosen values.

The tolerance of the nonlinear solver used to solve the implicit Euler method was set such that no instabilities appeared in the simulation. The same was done for the number of steps done by the nonlinear solver. In both models, the plate thickness and bending stiffness were set to a value that prevents off-plane buckling during the test. The width of the patch l_x is completely arbitrary and its length l_y is set according to the chosen aspect ratio.

In those tests, we want the behaviour to be quasi-static to reflect the experimental setup. Since ARCSim is a dynamic simulator, we had to choose the constraint velocity and the surface mass density low enough compared to the stiffnesses and size of the sample to make sure that the test was indeed quasi-static.

In addition to the previously mentioned parameters, the microscale model requires a target mesh resolution and a distance between barbs. The influence of those parameters on the stress-strain curves computed through simulation are studied in Figure 10. As those parameters go towards 0, the stress-strain curves approach a limit behaviour. While it would be natural to choose those parameters such we get close to the limit behaviour, we decided to choose higher values that give a good compromise between accuracy and time computation.

Similarly, for the macroscale model, we didn't choose a mesh resolution that would give a behaviour close to the limit one, instead we chose a lower (but still fine) resolution for the sake of time computation.

7.2 Deformation of a full feather

The parameter values we used for the figures involving the full feather are listed in Table 3. In what follows, we give the reasoning behind the chosen values.

The rachis parameters and bending parameters of the vane where chosen manually so that the behaviour of the full feather looks realistic. For their calibration, we used a scenario in which the base of the rachis of a feather is kept still while the tip of the rachis is pulled away from its rest state (see Figure 12).

7.2.1 Anisotropic membrane. The rachis stiffness was chosen following the measurement made in the literature which gives values in the order of 1 GPa. Its thickness was chosen such that off-plane buckling was prevented in the considered scenario while being as low as possible. For the vane, we decided on the smallest longitudinal bending modulus possible that avoids a buckling of the vane on the side away from the movement (see left of Figure 6). Then we picked the highest transverse bending modulus possible yielding wrinkles that looked sufficiently realistic visually (see Figure 6). Finally, we selected the smallest target edge length which gave a geometry close to the one seen in the deformation of a real feather.

7.2.2 Isotropic membrane. The parameters of the isotropic example in Figure 1 were chosen the same way. Hence, the rachis parameters are the same and the values of the other parameters have to be decided on independently of the other model. Since we are considering quasi-static deformations, only the ratio between the membrane Young modulus of this isotropic model and the bending moduli drives the geometry of the feather. Hence, we set this Young modulus to an arbitrary value and the Poisson ratio to 0 to have the same effect found in the real feather. The bending parameters are picked using the same process used for the calibration of the bending parameter of our anisotropic membrane model. The resulting difference observed between the bending parameters of the two models is expected due to the difference in membrane model.

7.2.3 Full bird. The full bird scenario shown in Figure 10 includes collisions between feathers. While collision resolution is out of the scope of our work, we wanted to make it perform as well as possible for this scenario. To do so, we sample the collision parameters and choose the ones that yields simulations with the less interpenetrations and instabilities. Despite this careful calibration of parameters, the nonlinear solver is sometime unable to converge for the chosen time-step size. This causes instabilities issues that can not be removed by increasing the precision of the sampling of the collision parameters. Instead, when the nonlinear solver is unable to reach convergence, the time-step is halved and time-stepping is retried recursively. This solves most difficulties due to collision, but some interpenetrations still remain. We leave their removal for future work.

8 ENERGY PENALTY FOR BENDING

Our membrane model is based on the St. Venant-Kirchhoff model, which is known to display non-physical behaviour and instabilities under large compressive strain [Sautter et al. 2022] (see Figure 7). For shells that uses a St. Venant-Kirchhoff membrane model, these issues rarely happen thanks to the fact that buckling appears before those problematic strains are reached. However, the high longitudinal bending modulus chosen to prevent the buckling of the vane in the previous section also unphysically prevents buckling under large compression. To enforce buckling under large compression and prevent the non-physical behaviour of the St. Venant-Kirchhoff model, we use the model of Kikuuwe et al. [2009] designed to prevent compression to zero volume.

$$\frac{1}{2}h\epsilon : \mathbf{E}(\theta) : \epsilon + h\frac{\kappa}{12}\left(\frac{1-J}{6}\right)^3, \tag{6}$$

where J is the determinant of the deformation gradient, and κ is a parameter of the model. This models adds the right term to the St. Venant-Kirchhoff model only under compression, this terms removes the instabilities and allows buckling if its parameter κ is chosen sufficiently high (see Figure 14).

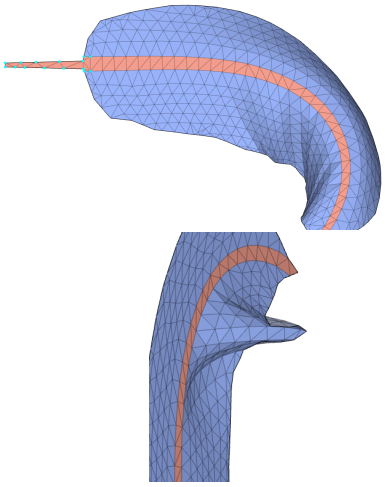

Figure 6: Using too small a longitudinal bending modulus can cause the vane to buckle during the deformation (top). Using too high a transverse bending modulus reduces the wave length of the wrinkles, making the deformation unrealistic (bottom).

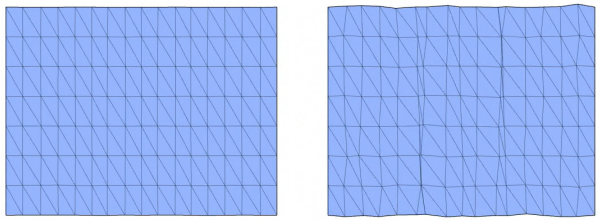

Figure 7: When compression reaches a certain point (left), elements whose elasticity follows the St. Venant-Kirchhoff model collapse to allow other elements to stretch (right).

The use of a log barrier instead of the cubic term has been considered. Such barrier diverges to infinity as λ approaches 0, this enforces buckling for any parameter chosen. However, the nonlinear solver becomes unable to converge on the time-stepping problem, hence our choice for the gentler cubic term.

9 CONSTRAINT IMPACT ON GEOMETRY

While we have shown through Figure 6 that stresses are incorrect when the constraint is not used in simulations with many elements, the geometric deformation produced by a simulation with no constraint might still be looking visually convincing. However, a simulation of the scenario of Figure 1 from the main document without the constraint shows major discrepancies (see Figure 13).

10 SENSITIVITY ANALYSIS

The transverse and shearing moduli of the macroscale model, E_{xy} and E_{yy}, are subject to variability, which comes from unavoidable variance among biological materials, and errors coming from multiple sources, which are: the imprecision in the measuring tools; human manipulation throughout the in-lab protocol; and divergence from the continuous model due to the numerical discretisation. In this section, we present a rough analysis of the impact of the variability and uncertainty on predicted stress and deformation. In the rest of this section, we denote variability and error together as variation.

For this analysis, we consider a simulation of the tilted scenario using the macroscale model. The value of the parameters of the simulation are listed in Table 2. Throughout the main document, we already use a stress measure given by Equation 2 in the main document. However, no measure of deformation is considered in the main document, so we need to introduce one. For this measure, we focus on the deflection of the sides of the tested sample (see Figure 9 in the main document). To simplify the evaluation of the impact of variation on this measure, we reduce it to a single scalar value $\bar{w}$ quantifying the average relative deflection.

To formally define $\bar{w}$, we represent the reference state of a tested sample using the set $\Omega = [0, l_x] \times [0, l_y]$, where l_x and l_y are respectively the width and length of the sample. When the sample is deformed, a point $(x, y) \in \Omega$ is displaced by $\mathbf{u}(x, y) = \begin{bmatrix} u_x(x,y) & u_y(x,y) \end{bmatrix}^T$ (see Figure 8). With these notations, the average relative change of width $\bar{w}$ is given by

$$\bar{w} = \frac{1}{l_y l_x} \int_0^{l_y} u_x(l_x, y) - u_x(0, y) \, \mathrm{d}y \,. \tag{7}$$

With this properly defined, we can now look at what influence a change of 10 % of both the transverse and shearing modulus has on these two measures. As can be seen in Figure 15, a change of 10 % of the transverse modulus E_{yy} has a minimal impact on forces (less than 2 % change), while its impact on the geometry is more substantial ($\approx$ 5 % change). The same changes in the shearing modulus have a similar impact on the geometry, whereas the impact on the forces is more substantial ($\approx$ 8.5 % change).

Parameter	Value
Number of elements	4×10^4
Aspect ratio $\frac{l_y}{l_x}$	1.38
Number of Newton iterations	50
Tolerance	1×10^{-7}
Time-step	0.02 s

Table 2: Parameters used for the sensitivity analysis.

11 MODIFICATIONS TO ARCSim

The implementation of our feather model required some modifications to ARCSim, that are listed below:

- Use of a nonlinear solver for the time-stepping problem (see section 3).
- Implementation of the non-extensibility constraint (see section 5).
- Possibility to have non-uniform orthotropy orientation. Previously, ARCSim considered the orientation of the fibers to

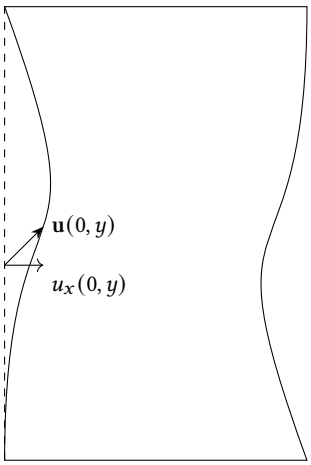

Figure 8: The deflection of the side of a deformed sample $u_x(0, y)$ is central to our measure of deformation described in section 10.

be uniform across the material. However, this does not hold for feathers (see Figure 12 top).

- Meshing algorithm which produces a mesh aligned with the orientation of highest stiffness, provided as input splines (see section 6)

Also, various changes were made to improve the quality and usability of the simulations generated by ARCSim.

- Reduced gradient method for handling of linear constraints. Previously, linear equality constraint were solved through the addition of penalisation energies to the physics. Instead, we used a reduced gradient method that solves the nonlinear optimisation problem directly within the space of values verifying the constraint. Some details on reduced gradient method can be found in Bartholomew–Biggs [2008].
- It is now possible to export data at each time-steps within a JSON file. The exported data is configurable through the configuration file.

12 LIMITATIONS

While we have compared the microscale model with multiple experiments, we chose to show only one of them in Section 8 of the main document to prevent an overload of information for the reader. As mentioned in our main paper, this choice was made on an experiment where the feather behaves purely elastically. However, we noted that among all our experiments performed, this was not always the case. The appearing of non-elastic events in some experiments brings to light a limitation of our elastic feather model. Hence, we provide here more data that allows to discuss this issue more thoroughly.

As we can see from the main document, our microscale model predicts well the stress-strain curves of some experiments, however, other experiments have their measured stress lower than the prediction of our model (see Figure 11). This lower stress can be explained by the presence of non-elastic events in the experiments. In those, the barbules rearrange themselves, allowing stress to dissipate (see Figure 9).

REFERENCES

Michael Bartholomew–Biggs. 2008. *Linear Equality Constraints*. Springer US, 1–14. https://doi.org/10.1007/978-0-387-78723-7_17

Franco Brezzi and Michel Fortin. 1991. *Mixed and Hybrid Finite Element Methods*. https://api.semanticscholar.org/CorpusID:120233740

Dominique Chapelle. 1995. *Etude numérique du verrouillage de quelques méthodes d'éléments finis pour les coques*. Research Report RR-2740. INRIA. https://inria.hal.science/inria-00073953 Projet MODULEF.

Ryo Kikuuwe, Hiroaki Tabuchi, and Motoji Yamamoto. 2009. An edge-based computationally efficient formulation of Saint Venant-Kirchhoff tetrahedral finite elements. *ACM Trans. Graph.* 28, 1, Article 8 (feb 2009), 13 pages. https://doi.org/10.1145/1477926.1477934

Rahul Narain, Armin Samii, and James F. O'Brien. 2012. Adaptive anisotropic remeshing for cloth simulation. *ACM Transactions on Graphics* 31, 6 (Nov. 2012), 1–10. https://doi.org/10.1145/2366145.2366171

Klaus Bernd Sautter, Manuel Meßmer, Tobias Teschemacher, and Kai-Uwe Bletzinger. 2022. Limitations of the St. Venant–Kirchhoff material model in large strain regimes. *International Journal of Non-Linear Mechanics* 147 (Dec. 2022), 104207. https://doi.org/10.1016/j.ijnonlinmec.2022.104207

Jonathan Richard Shewchuk. 1996. Triangle: Engineering a 2D quality mesh generator and Delaunay triangulator. In *Applied Computational Geometry Towards Geometric Engineering*, Ming C. Lin and Dinesh Manocha (Eds.). Springer Berlin Heidelberg, Berlin, Heidelberg, 203–222.

Andreas Wächter and Lorenz T. Biegler. 2006. On the implementation of an interior-point filter line-search algorithm for large-scale nonlinear programming. *Mathematical Programming* 106 (2006), 25–57. https://api.semanticscholar.org/CorpusID:14183894

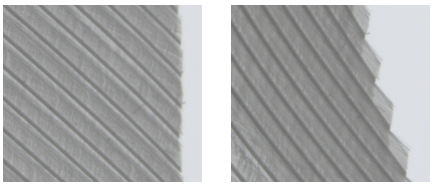

(a) Non-elastic behaviour

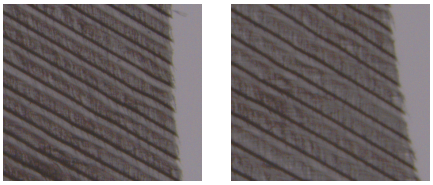

(b) Elastic behaviour

Figure 9: Photographs of two tilted traction tests zoomed on the side of the tested sample. The sample shown in the subfigure 9a displays a non-elastic behaviour. In its rest state (left) the edge of the sample is smooth, after extension (right) the edge has become ragged due to a rearrangement of the barbules. This rearrangement dissipates the bending energy of the barbules, allowing the samples to reach a lower energy state. The subfigure 9b presents a sample in which none of those rearrangements take place, as can be seen by the smooth sample edge even after extension.

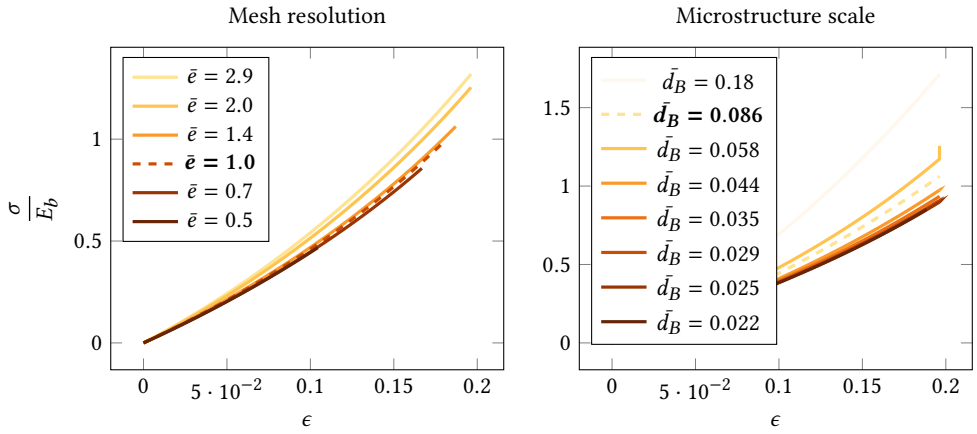

Figure 10: Non-physical parameters influence on simulation results shown through non-dimentionalised stress strain curves. This data was obtained by simulating the tilted scenario with an angle of 45° on sample with aspect ratio $a = \frac{l_y}{l_x} = 1.3$, a barb surface density of $\Phi_B = \frac{w_B}{d_B} = 0.16$ and a Young's modulus ratio of $\frac{E_b}{E_B} = 10^{-6}$. The left curves were obtained by fixing the non-dimentionalised inter barbs distance to $\bar{d}_B = \frac{d_b}{l_y} = 0.086$ and varying the ratio between element edge size and barbs width $\bar{e}$. The right curves were obtained by fixing the non-dimentionalised edge size to $\bar{e} = 2.9$ and varying the non-dimentionalised inter barbs distance $\bar{d}_B$. As expected, as the edge size goes toward zero, the stress-strain curve reach a limit which is the continuous solution of the solved problem. Also, as the inter-barbs distance is decreased the curve reaches the limit that is the homogenized solution of the problem. The values we used in the main paper figures are shown in bold in the legend.

Parameter	Value
Feather length	0.2 m
Tolerance	10^{-7}
Number of Newton steps	50
Target element edge length	5×10^{-3} m
Isotropic longitudinal bending modulus $EI_{\perp}$	7.9×10^{-4} N m
Isotropic transversal bending modulus $EI_{\|\|}$	2.5×10^{-8} N m
Anisotropic longitudinal bending modulus $EI_{\perp}$	2.5×10^{-4} N m
Anisotropic transverse bending modulus $EI_{\perp}$	10^{-7} N m
Barrier coefficient κ (see section 8)	5.04×10^{7} N m^{-1}
Surface mass density	2.6×10^{-2} kg m^{-2}
Rachis Young's modulus	10^{9} Pa
Rachis thickness	3×10^{-3} m
Rachis Poisson's ratio	0.49
Rachis surface mass density	0.54 kg m^{-2}
Time-step	0.011 s

(a) Parameters for Figure 1.

Parameter	Value
Feather length	0.2 m
Target element edge size	5×10^{-3} m
Surface mass density	2.6×10^{-2} kg m^{-2}
Longitudinal bending modulus $EI_{\perp}$	2.5×10^{-4} N m
Transverse bending modulus $EI_{\|\|}$	1×10^{-7} N m
Barrier coefficient κ (see section 8)	5.04×10^{7} N m^{-1}
Rachis Young's modulus	1×10^{9} N m^{-2}
Rachis thickness	3×10^{-3} m
Rachis Poisson's ratio	0.49
Rachis surface mass density	0.54 kg m^{-2}
Time-step	0.0028 s
Repulsion thickness	10^{-3} m
Collision stiffness	10^{11} J m^{-2}

(b) Parameters for Figure 10.

Table 3: Parameters used for generating the figures involving the full feather in the main document. Parameters whose value can be inferred from the from the main document are not listed. If a notation was given in the main document for a parameter, we recall this notation in the table.

Parameter	Value
Tolerance	10^{-20}
Surface mass density	$10^{-9}\,\mathrm{kg\,m^{-2}}$
Bending stiffness $EI_{\perp}, EI_{\|\|}$	$10\,\mathrm{N\,m}$
Number of Newton steps	50
Shearing modulus E_{xy}	$1\,\mathrm{N\,m^{-2}}$
Transverse modulus E_{yy}	$1\,\mathrm{N\,m^{-2}}$
Velocity	$0.12\,\mathrm{m\,s^{-1}}$
Width l_x	$1\,\mathrm{m}$
Aspect ratio $\frac{l_y}{l_x}$	1.3
Time-step	0.01 s

(a) Parameters for Figure 5.

Parameter	Value
Number elements	128×10^3
Surface mass density	$10^{-5}\,\mathrm{kg\,m^{-2}}$
Bending stiffness $EI_{\perp}, EI_{\|\|}$	$10\,\mathrm{N\,m}$
Shearing modulus E_{xy}	$1\,\mathrm{N\,m^{-2}}$
Longitudinal modulus E_{xx}	$10^4\,\mathrm{N\,m^{-2}}$
Transverse modulus E_{yy}	$1\,\mathrm{N\,m^{-2}}$
Velocity	$0.12\,\mathrm{m\,s^{-1}}$
Width l_x	$1\,\mathrm{m}$
Aspect ratio $\frac{l_y}{l_x}$	1.3
Time-step	0.01 s

(b) Parameters for Figure 6.

Parameter	Value
Non dimentionalised barbs distance $\bar{d_B}$	0.086
Non dimentionalised edge size $\bar{e}$	1.0
Number of Newton iterations	4
Thickness h	$1\,\mathrm{m}$
Tolerance	10^{-15}
Time-step	0.01 s

(c) Parameters for Figure 11.

Parameter	Value
Number elements	4×10^4
Aspect ratio $\frac{l_y}{l_x}$	1.38
Number of Newton iterations	50
Tolerance	10^{-7}
Time-step	0.02 s

(d) Parameter for Figure 6

Table 4: Parameters used for the generation of the figures involving the traction test in the main document. Parameters whose value can be inferred from the main document are not listed. If a notation was given in the main document for a parameter, we recall this notation in the table.

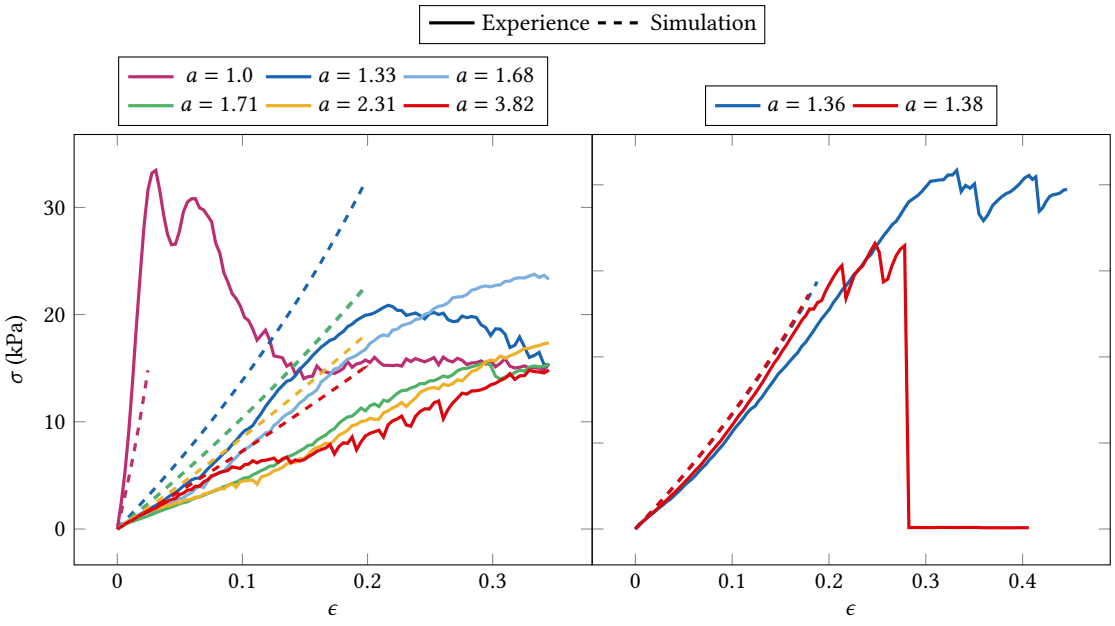

Figure 11: Comparison of the microscale model with experiments on the tilted traction scenario. In some of those experiments, the barbules rearrange themselves, see Figure 9. Since our model is completely elastic, it is unable to take into account such events. Due to the rearrangement of the barbules, stress is dissipated. Hence, the stress predicted by our model is higher than the measured stress (left). Other experiments do not have any of these barbules rearrangements, this allows our model to predict properly their measured stress-strain curves (right).

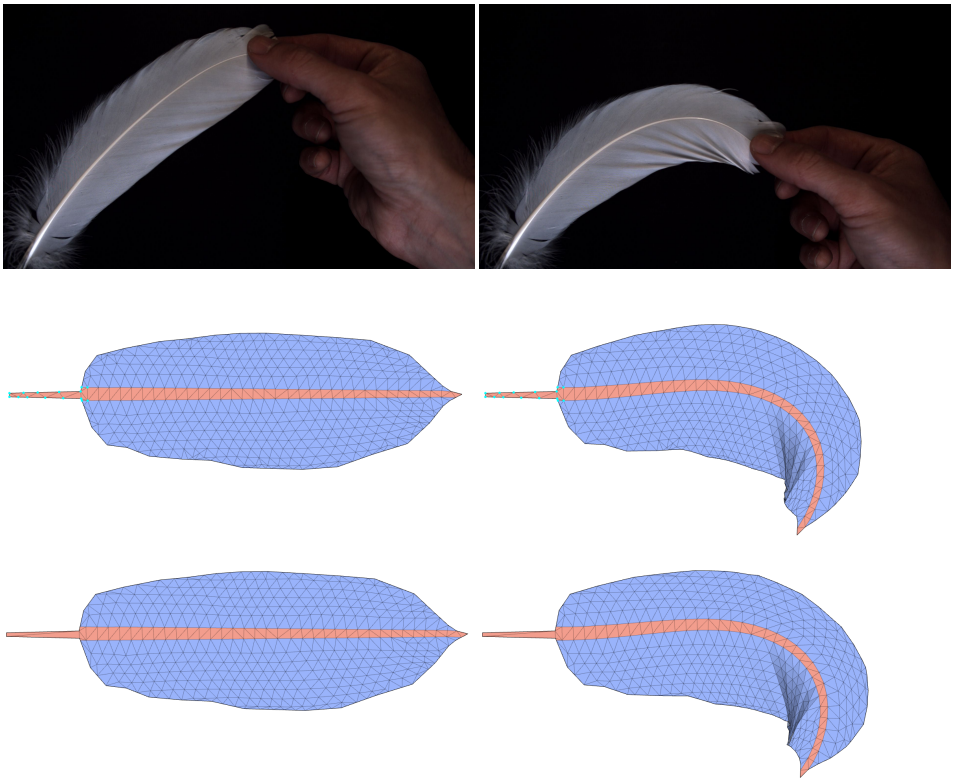

Figure 12: Scenario where the rachis of a feather is held at its base and pulled at its tip. This scenario was performed with a real feather (top) and within the simulation using an isotropic membrane model (middle) and our anisotropic membrane model (bottom). This scenario was used to select the physical parameters of the rachis model and vane bending model.

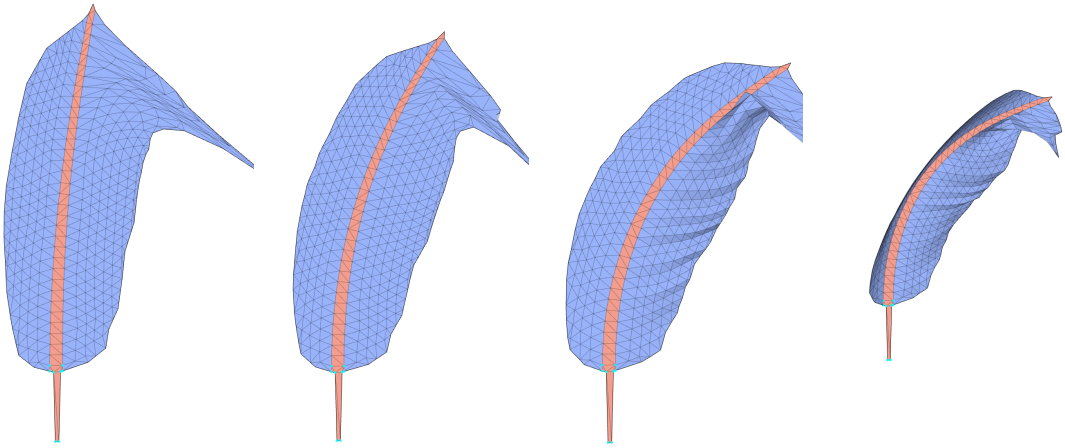

(a) $\frac{E_{xx}}{E_{yy}} = 10^1$ **(b)** $\frac{E_{xx}}{E_{yy}} = 10^2$ **(c)** $\frac{E_{xx}}{E_{yy}} = 10^3$ **(d)** $\frac{E_{xx}}{E_{yy}} = 10^4$

Figure 13: Simulation of the scenario of Figure 1 in the main document with the inextensibility constraint removed. From left to right, results are shown when increasing the value of the coefficient E_{xx}, which has an influence on the behaviour of the vane when the constraint is inactive.

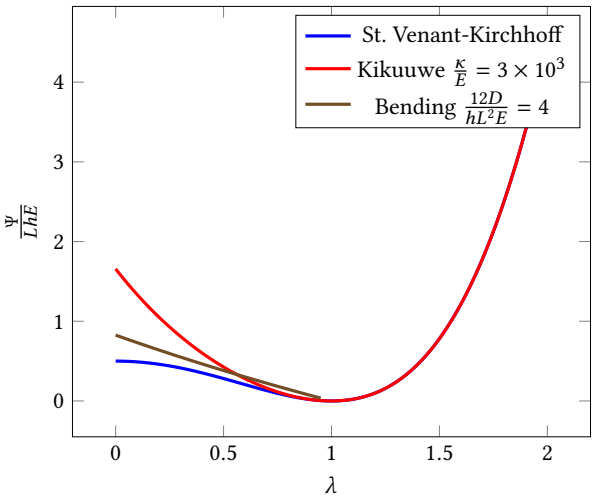

Figure 14: Internal energy Ψ of a one dimensional truss of length L and thickness h. The endpoints of the truss are moved away and brought close to each other. The distance between the endpoints relative to the distance at rest is denoted by λ. The displayed curves are the internal energy when no buckling occurs for both the St. Venant-Kirchhoff model (——) $\frac{1}{2}LhE(\lambda^2-1)^2$ and the Kikuuwe model (——) $\frac{1}{2}LhE(\lambda^2-1)^2 + Lh\frac{\kappa}{12}\left(\frac{1-\lambda}{6}\right)^3$, as well as the bending energy for an isometric deformation (——) $\frac{1}{2}\int_0^L D\kappa^2 \, \mathrm{d}s$ where D is the bending modulus and κ is the curvature. This last curve was computed through ARCSim's finite element simulation. When the membrane behaviour is modeled with the St Venant-Kirchhoff and the bending modulus is large, buckling does not occur under compression as it would not reduce the internal energy of the truss. In contrast, with the Kikuuwe model, a sufficiently large coefficient κ induces a membrane energy that is higher than the bending energy under compression, allowing buckling to emerge.

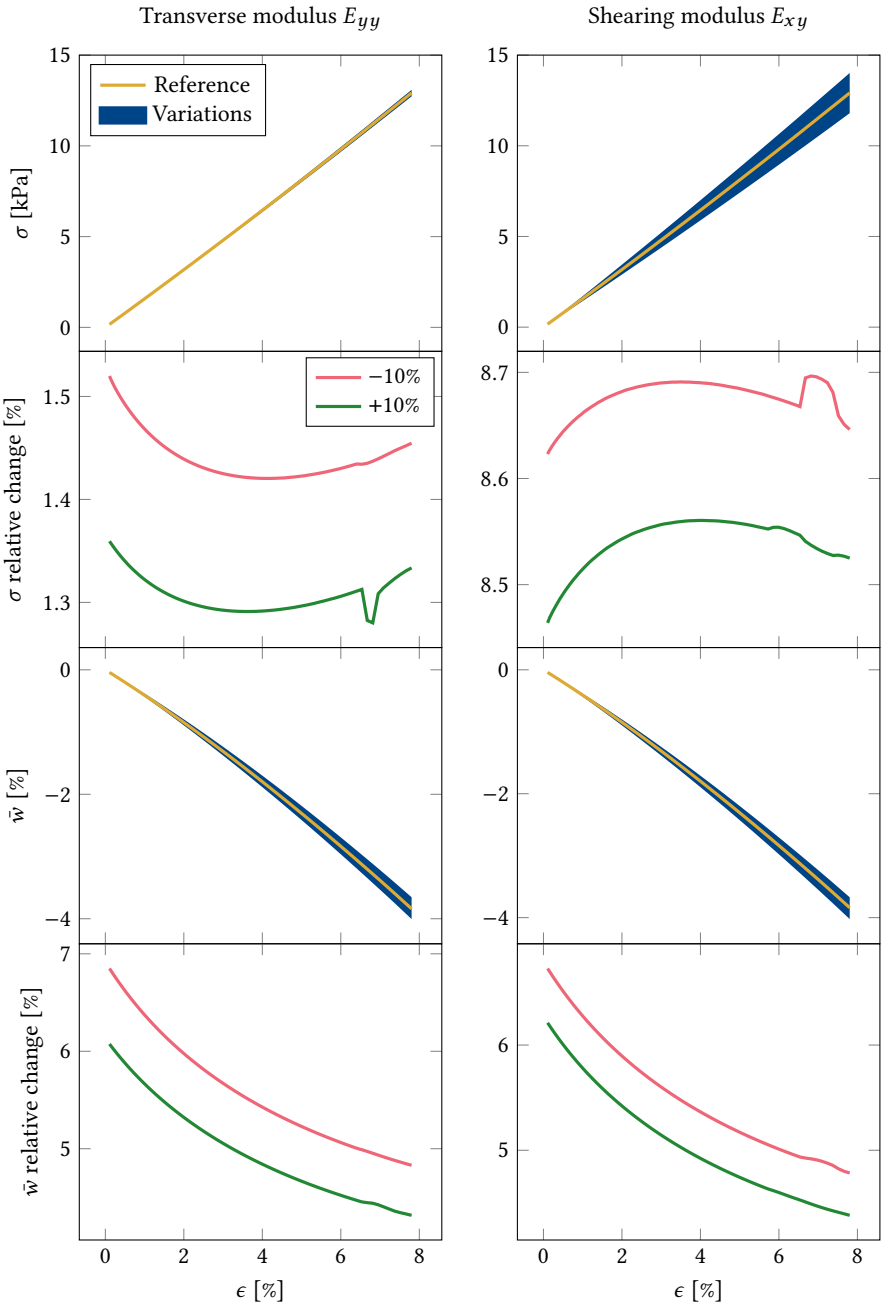

Figure 15: Impact of a variation of 10 % in the transverse modulus E_{yy} (left) and in the shearing modulus E_{xy} (right) on measured stress σ (top) and measured average relative width change $\bar{w}$ (bottom) in a tilted traction test simulation. For each considered parameter and variations, we show the reference value (——) with the area spanned by the measure due to the considered variation of the modulus (■), in another set of axis we show relative change in the measure due to an increase of the modulus (——) or a decrease (——).